Dual Floating based Three Port DC-DC Converter for EV-APM

Huu-Phuc Kieu, *Member*, *IEEE*, Ngoc-Quy Do, and Sewan Choi, *Fellow, IEEE*

***Abstract*—This article proposes a new isolated three-port DC-DC converter (TPC) named dual floating dual active bridge (DAB) three-port converter. The proposed converter combines an isolated DAB converter and an interleaved non-isolated dual floating boost (DFB) converter. As the power demand of auxiliary loads in the vehicles rapidly increases due to autonomous and entertainment systems, a dual auxiliary voltage (48V and 12V) system is introduced to mitigate the burden of high current. The high voltage gain feature of the DFB converter ensures that the operating duty remains around 0.5, reducing filter size, turn-off current, and circulating current, and increasing the power transfer capability from the high voltage side. Additionally, the lower voltage stress on the low-side switches allows for the use of switches with lower $R_{DS,on}$, reducing conduction losses. To validate the theoretical claims, a 6.1kW, 100kHz prototype of the proposed TPC has been built. The prototype operates with a wide HV-port voltage range of 400V-840V and a 12V-port voltage range of 9V-16V while providing a fixed 48V to the 48V-port. The prototype achieves a power density of 9.14kW/L and a peak efficiency of 96.6%.**

***Index Terms*—Auxiliary power module, dual auxiliary voltage, electric vehicles, high power density, 800V battery, zero voltage switching, three-port converter.**

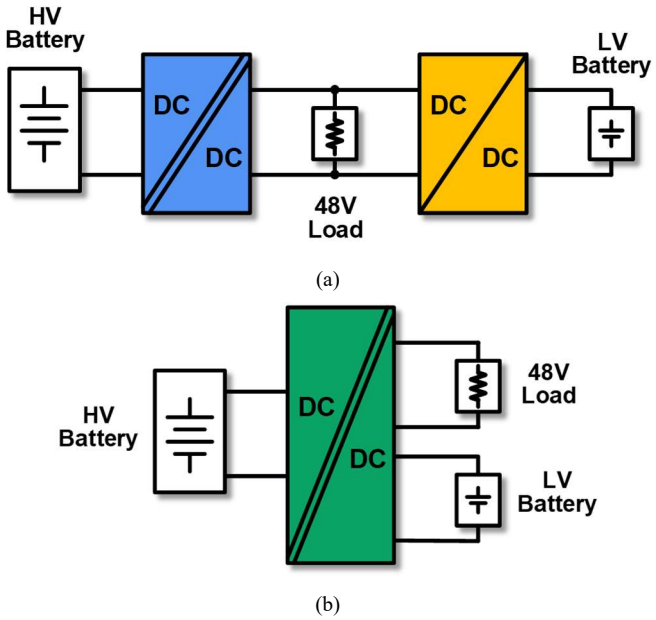

Fig. 1 Dual auxiliary voltage system in EV application. (a) Conventional separated two converters. (b) Proposed three-port converter.

I. Introduction

Nowadays, the electric vehicles (EVs) market is rapidly increasing due to EVs' potential for reducing greenhouse gas emissions. However, the space under the hood in EVs is limited. Therefore, the power converters in EVs must be highly efficient and compact [1]. The auxiliary power module (APM) is one of the crucial power converters in EVs [2-4]. The APM receives power from the high-voltage (HV) battery to charge the low-voltage (LV) battery and provide power to auxiliary loads. It needs to handle a wide range of input and output voltages, as well as output high current. For the 400V HV battery class, the APM needs to operate an input from 250 to 450 V, while for the 800V class, it requires an input range of 400 to 840V. The output voltage varies from 9 to 16V, with a high output current [5-11].

As more auxiliary loads are implemented in EVs, such as autonomous systems and entertainment systems, higher-power APMs are required [10-11]. With the increasing power demand of auxiliary loads reaching up to 6kW, the output current exceeds 500A with only a 12V voltage system. This results in high conduction loss, reducing the efficiency and necessitating large, costly wires. This is a challenge for future EVs, as the heavier auxiliary load current causes high power loss in wire harnesses of the APM.

To reduce the burden of high current, a dual auxiliary voltage architecture is introduced, as shown in Fig. 1, suggesting 12V and 48V (considering that voltages above 60V can generate shocks according to safety standards IEC 479-1). Due to the use of dual auxiliary voltage systems, an additional converter is required, which increases the size and cost of the systems, as shown in Fig. 1(a) [12]. Therefore, to reduce the size and cost of the dual low auxiliary systems, auxiliary power modules (APMs) are considering the three-ports DC-DC converter shown in Fig. 1(b) [13-23]. An auxiliary power module of electronic vehicles (EVs) can control several ports (such as HV, 48V, and 12V) within a single circuit. Meanwhile, conventional systems use separated isolated converters for each 800V-48V power line [24-28] and non-isolated converters for each 48V-12V power line [29-32]. Therefore, a triple active bridge (TAB) converter was introduced to reduce the components and size of the systems [17],[22-23]. In the TAB converter, the ports are isolated. Since the power transfer from HV-port to 12V-port became a single-stage conversion, the efficiency is increased. However, the power transfer between ports in the TAB converter is coupled. Therefore, a complex control block diagram is required to decouple power transfer. To address this issue, a

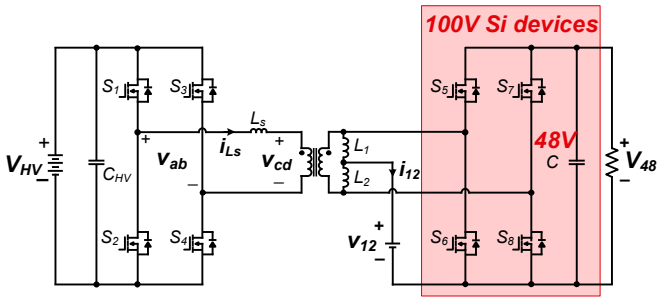

(a)

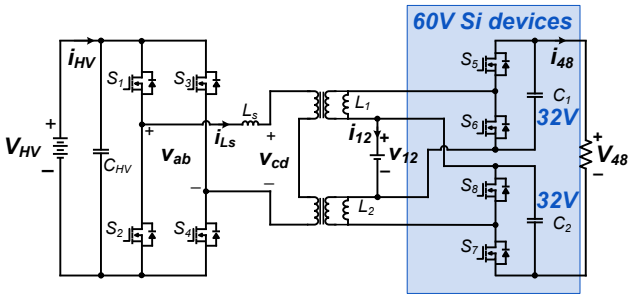

(b)

Fig. 2 Three port topologies for dual auxiliary voltage EV systems: (a) conventional current fed DAB topology [14-15], (b) proposed three port topology [19].

TABLE I.
VOLTAGE GAIN BETWEEN LV PORTS (48V AND 12V)

	Voltage gain
Conventional	$\frac{1}{1-d_B}$
Proposed	$\frac{1+d_B}{1-d_B}$

dual-transformer concept TAB is introduced [21]. Since the power can be controlled separately by the duty cycle and phase shift, a complex control block diagram for decoupling is not required. However, the TAB converter requires a high-current three-winding transformer. Additionally, EV applications do not require isolation between dual auxiliary voltage ports. Therefore, other previous lectures proposed a multi-port DC converter that integrates a non-isolated buck-boost converter and an isolated DAB converter [13-15], [18-20]. Due to the required high voltage gain from 12V to 48V with the conventional buck-boost converter [13-15], the duty cycle range of the low side is far from 0.5 (0.67-0.81 duty range equivalent with 9V-16V 12V-port voltage range), increasing the filter size, circulating current, and reducing the power transfer capability of the DAB converter. To solve this problem, a series-capacitor high-step-ratio buck-boost converter [33] is combined with an isolated DAB converter [20]. With the high step ratio, the operating duty range is around 0.5 (0.37 – 0.67 equivalent to 9V-16V). However, designing a high-current series capacitor on the low-voltage side is challenging because it requires high-power operation.

TABLE II
DESIGN SPECIFICATIONS FOR DUAL LOW VOLTAGE EVs

Item		Values
HV-port Power	P_{HV}	6.1 kW
48V-port Power	P_{48}	4 kW
12V-port Power	P_{12}	2.1 kW
HV-port voltage	V_{HV}	400 ~ 840 V
12V-port voltage	V_{12}	9 ~ 16 V
Maximum current in 12V port	$I_{12,max}$	150 A
Switching frequency	f_s	100 kHz
Peak efficiency	η	95%
Power density	-	> 8 kW/L

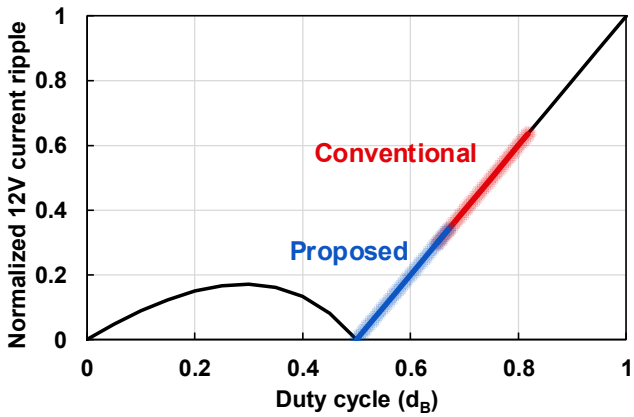

Fig. 3 Normalized 12V-port current ripple versus duty cycle.

In this paper, a new isolated dual floating current DAB converter is proposed, providing two output voltages to reduce the cost and volume. The proposed topology combines a non-isolated dual floating boost converter [34] and a DAB converter. The proposed converter has the following features:

1) The proposed three-port converter structure reduces the number of components compared to the conventional separated two converters, consequently reducing the size and cost of the system.
2) A high step-up ratio, with an operating duty range closed to 0.5 (0.5-0.68) helps reduce the ripple current in 12V port, minimizes circulating current, and extends the period of transfer power.
3) Lower voltage stress on the low-side switches allows the use of lower $R_{DS,on}$ switches, resulting in reduced conduction loss.
4) All switches in the converter can achieve zero-voltage switching (ZVS) turn-on under the entire voltage and power range.

A 6.1kW, 100kHz prototype of the proposed converter has been built and tested to validate the proposed concepts. The prototype achieves a power density of 9.14kW/L and a peak efficiency of 96.6%.

II. PROPOSED DOUBLE FLOATING BASED DAB CONVERTER

In EV applications, the dual auxiliary voltage ports do not require isolation. The three-port current-fed DAB converter is suitable for dual auxiliary voltage applications due to its reduced component count and simplicity of control, as shown

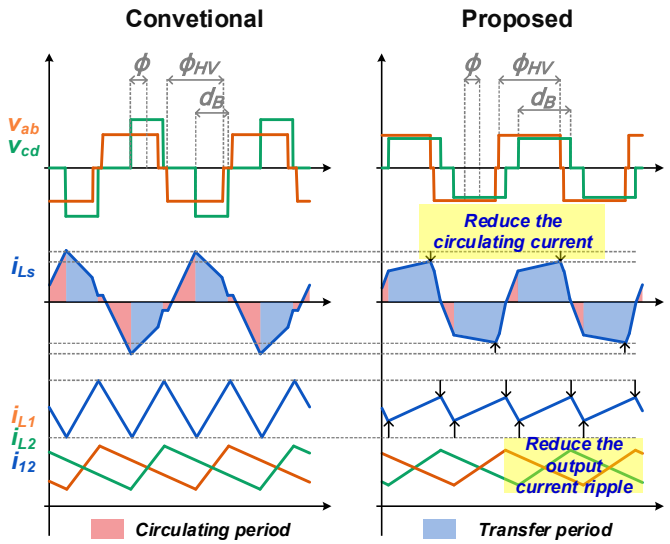

Fig. 4 Comparisons of conventional TPC with proposed TPC.

in Fig. 2(a). However, the high ratio of auxiliary voltages (4 at 48V and 12V), necessitates a low-side operating duty cycle far from 0.5. In this section, a new TPC is proposed, and its operating principle also is presented.

A. Features of Proposed Double Floating Based DAB Converter

Fig. 2(a) shows the conventional current-fed DAB converter, widely used for three-port systems due to its ability to operate over a wide voltage range and reduce the number of components [14-15]. The converter is a combination of an interleaved buck-boost converter and a DAB converter. In [14], the conventional current-fed DAB converter was used for a three-port DC-DC converter designed for dual auxiliary voltage in EV applications. However, the requirement of the dual auxiliary voltages of 12V and 48V necessitates a low side voltage duty cycle far from 0.5 (0.71), leading to a required large filter due to the high output current ripple. To address this issue, Fig. 2(b) shows the proposed converter, which combines a non-isolated dual floating boost converter with a DAB converter. The high step-up voltage gain of the non-isolated dual floating boost converter [30] brings the required low-side duty cycle closer to 0.5 (0.6), reducing the size of the filter inductor. A comparison of the voltage gain between LV ports of the conventional and proposed converter can be seen in TABLE I.

Fig. 3 compares the normalized 12V-port current ripple between conventional and proposed converters, considering the specification in TABLE II. The proposed converter, with its higher voltage gain, shifts the operating duty cycle from 0.67-0.81 to 0.5-0.68, close to 0.5. The results demonstrate that the proposed converter has a smaller 40% output current ripple. Additionally, the voltage stress on the LV side switches is reduced from 48V to 32V, allowing the use of lower $R_{DS,on}$ switches, as shown in Fig. 2, thereby, reducing conduction loss. Fig. 4 shows the key waveform comparison of the conventional and proposed converters. Both topologies have the same control variables. On the HV side, the high voltage

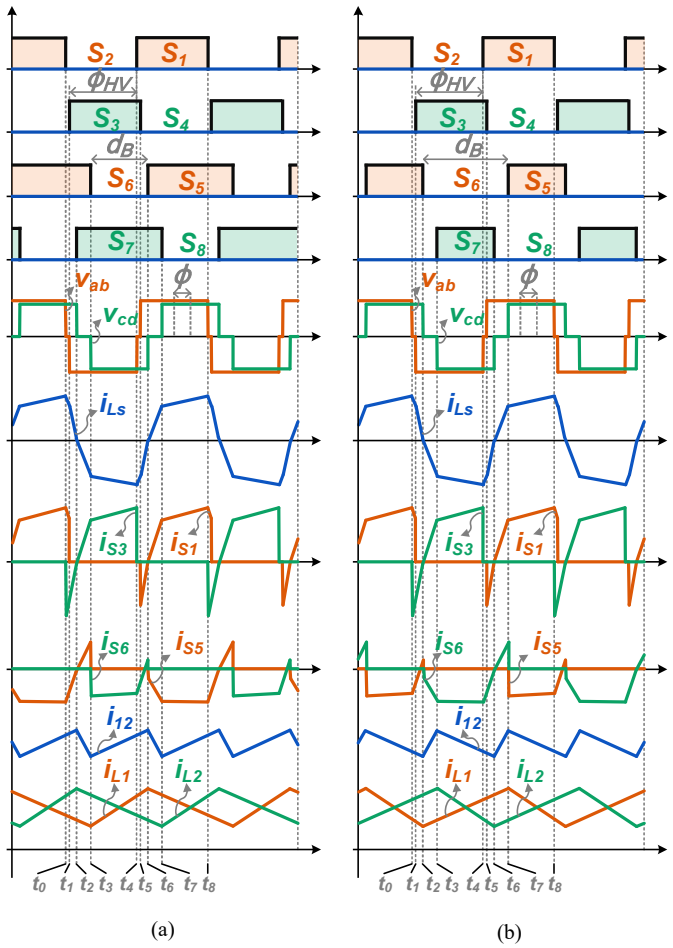

Fig. 5 Theoretical key operation waveforms in (a) $d_B < 0.5$, $d_B \geq 0.5$.

phase shift (ϕ_{HV}) between high voltage side legs can be adjusted to achieve ZVS over a wide voltage range. The duty cycle (d_B) can be varied to regulate the voltage ratio between the 12V port and 48V ports, determining the power direction between these ports. The phase shift between the HV side and LV side (ϕ) controls power transfer between the two sides. When $\phi > 0$, power is transferred from the HV side to the LV side, and when $\phi < 0$, power is transferred from the LV side to the HV side. Since the operating duty is around 0.5, the zero voltage level is smaller, resulting in a reduced circulating current period and an increased power transfer period, as shown in Fig. 4. Consequently, this reduces the RMS current and peak current of the devices, significantly reducing both the switching and conduction loss.

B. Operation Principle of Proposed Converter

In this APM application, HV port and LV port are connected to batteries and the 48V port is required to be constant 48V. The voltage ratio between 12V port and 48V port is duty (d_B), as shown in Table I. The HV phase shift (ϕ_{HV}) is fixed under voltage conditions for achieving ZVS turn on is described in chapter IV. The power control between HV side and LV side is phase shift (ϕ).

The proposed converter can divide into 2 separate operating conditions according to the LV duty cycle (d_B) with $d_B < 0.5$ and $d_B \geq 0.5$, as shown in Fig. 5. In this article, the operating

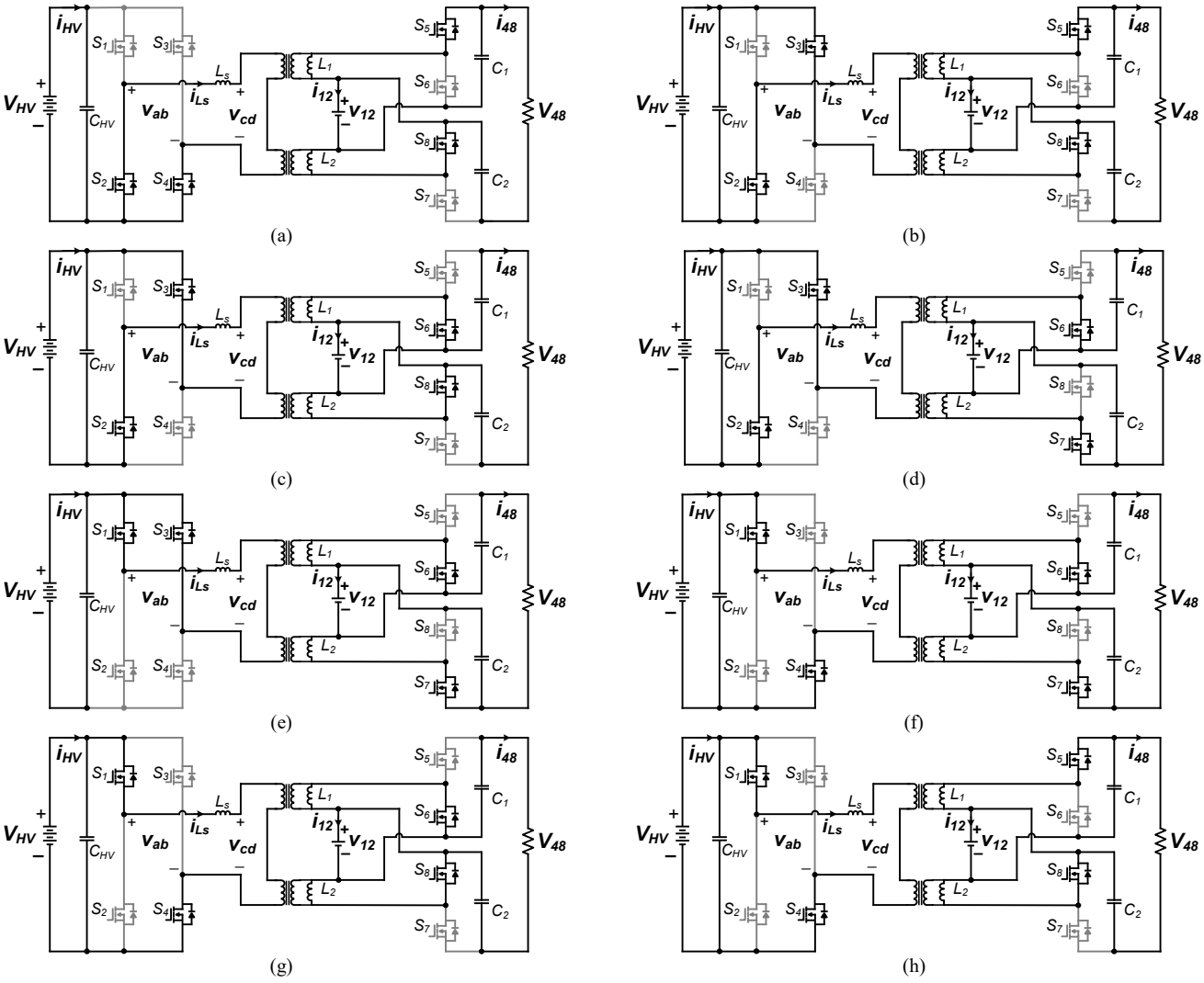

Fig. 6 Operation modes of the proposed converter (a) *Mode 1*, (b) *Mode 2*, (c) *Mode 3*, (d) *Mode 4*, (e) *Mode* 5, (f) *Mode 6*, (g) *Mode 7*, (h) *Mode 8.*

duty range is larger than 0.5. Therefore, the detailed operating analysis is considered $d_B \geq 0.5$. With $d_B < 0.5$, it can be analyzed in the same way. To simplify the steady-stage operation analysis of the proposed converter, the following assumptions are made:

1) The parasitic capacitor of the switches is neglected.
2) The output capacitors of each port are large enough that can be considered as constant voltage sources during a switching period.
3) All the passive components are ideal, meaning parasitic effects (such as parasitic resistance, inductance, and capacitance) are not taken into account.

With the above assumptions, the operation can be divided into 8 modes in one switching cycle, as shown in Fig. 6. The operation modes of the proposed converter are described as follows.

Mode 1 ($t_0 - t_1$): $S_{2,4,5,8}$ are ON, and the HV side winding is short-circuited through $S_{2,4}$, and therefore, $v_{ab} = 0$. L_1 releases power to the 48V-port, while L_2 continues to be energized. In this mode, the series inductor current i_{Ls} is expressed as

$$i_{Ls}(t) = i_{Ls}(t_0) + \frac{-N(V_{C1})}{L_s}(t - t_0) \tag{1}$$

where N is the turn ratio of the transformer.

Mode 2 ($t_1 - t_2$): At t_1, the series inductor (L_s) current is positive, so the switch S_3 is turned on with ZVS. The HV side voltage is provided reversely by HV-port, $v_{ab} = -V_{HV}$, and the series inductor current i_{Ls} is expressed as

$$i_{Ls}(t) = i_{Ls}(t_1) + \frac{-V_{HV} - N(V_{C1})}{L_s}(t - t_1) \tag{2}$$

Mode 3 ($t_2 - t_3$): S_5 and S_6 are turned off and on, respectively. $L_{1,2}$ continue to be energized. L_1, and L_2 are energized linearly with applied voltage V_{12}. In order to achieve ZVS turn on for S_6, it must satisfy condition (3) and the series inductor current i_{Ls} is expressed as (4).

$$N \cdot i_{Ls}(t_2) - i_{L1}(t_2) < 0 \tag{3}$$

$$i_{Ls}(t) = i_{Ls}(t_2) + \frac{-V_{HV}}{L_s}(t - t_2) \tag{4}$$

Mode 4 ($t_3 - t_4$): S_8 and S_7 are turned off and on, respectively. L_1 releases power to the 48V-port, while L_2

TABLE III
COMPARISON OF COMPONENTS RATINGS AND DESIGN PARAMETERS

Item	Conventional	Proposed
High side (S_1~S_4)	AIMCQ120R030M1T (Infineon) 1200 V / 30 mOhm	AIMCQ120R030M1T (Infineon) 1200 V / 30 mOhm
Low side (S_5~S_{12})	IAUS300N10S5N015T (Infineon) 100 V / 1.5 mOhm	IAUTN06S5N008T (Infineon) **60 V / 0.8 mOhm**
Turn ratio	5 : 1	6 : 1
L_s	12 μH	12 μH
L_1, L_2, L_3, L_4	1.1 μH	**0.7 μH**
C_{HV}	C4AQNBU4170M1WJ (3ea) 1 kV / 1.7 μF	C4AQNBU4170M1WJ (3ea) 1 kV / 1.7 μF
C	C2220C226M5R2CAUTO (16ea) 50 V / 22 μF	-
C_1, C_2	-	C2220C226M5R2CAUTO (8ea) 50 V / 22 μF

continues to be energized. In this mode, the series inductor current i_{Ls} is expressed as

$$i_{Ls}(t) = i_{Ls}(t_3) + \frac{-V_{HV} + N(V_{C2})}{L_s}(t - t_3) \tag{5}$$

Mode 5 (t_4 – t_5): At t_4, the switch S_3 is turned off, and the series inductor current is negative, so the switch S_4 is turned on with ZVS. The HV side winding is short-circuited through $S_{2,\ 4}$, and therefore, v_{ab} = 0. The inductor current can be expressed as follows

$$i_{Ls}(t) = i_{Ls}(t_4) + \frac{N(V_{C2})}{L_s}(t - t_4) \tag{6}$$

Mode 6 (t_5 – t_6): S_2 is turned off and S_1 is turned on with ZVS, respectively. The HV side voltage is provided by HV-port, v_{ab} = V_{HV}. L_2 continues power to the 48V-port, while L_1 continues to be energized. The inductor current is expressed as

$$i_{Ls}(t) = i_{Ls}(t_5) + \frac{V_{HV} + N(V_{C2})}{L_s}(t - t_5) \tag{7}$$

Mode 7 (t_6 – t_7): S_7 and S_8 are turned off and on, respectively. L_1 and L_2 are energized with applied voltage V_{12}. In this mode, the inductor current is expressed as

$$i_{Ls}(t) = i_{Ls}(t_6) + \frac{V_{HV}}{L_s}(t - t_6) \tag{8}$$

Mode 8 (t_7 – t_8): *At t7,* S_6 is turned off and S_5 is turned on with ZVS. L_1 power to the 48V-port, while L_2 continues to be energized. The HV side voltage is provided by HV-port, v_{ab} = V_{HV}.

$$i_{Ls}(t) = i_{Ls}(t_7) + \frac{V_{HV} - N(V_{C1})}{L_s}(t - t_7) \tag{9}$$

The period of each mode can be expressed as follows:

$$\begin{cases} T_5 = T_1 = t_5 - t_4 = t_1 - t_0 = (0.5 - \phi_{HV})T_s \\ T_6 = T_2 = t_6 - t_5 = t_2 - t_1 = 0.5 \cdot (-1 + 3\phi_{HV} - d_B + 2 \cdot \phi)T_s \\ T_7 = T_3 = t_7 - t_6 = t_3 - t_2 = (-0.5 + d_B)T_s \\ T_8 = T_4 = t_8 - t_7 = t_4 - t_3 = (1 - 0.5 \cdot \phi_{HV} - 0.5 \cdot d_B - \phi)T_s \end{cases} \tag{10}$$

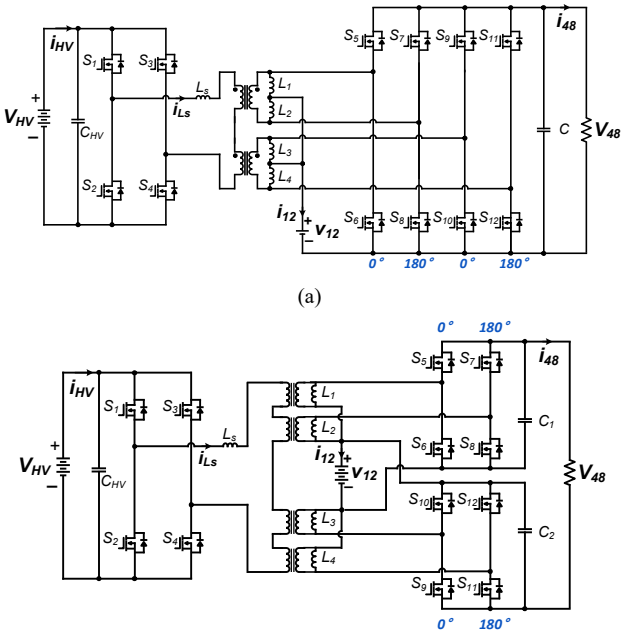

Fig. 7 Multi-legs LV side for high current opeartion. (a) Conventional converter, (b) Proposed converter.

The instant currents of L_s are expressed as follows:

$$i_{Ls}(t_0) = \frac{1}{2}\left(\frac{V_{HV}}{L_s}\phi_{HV} + \frac{N \cdot V_C}{L_s}(-1 + \phi_{HV} + 2 \cdot \phi)\right)T_s \tag{11}$$

$$i_{Ls}(t_1) = \frac{1}{2}\left(\frac{V_{HV}}{L_s}\phi_{HV} + \frac{N \cdot V_C}{L_s}(-2 + 3 \cdot \phi_{HV} + 2 \cdot \phi)\right)T_s \tag{12}$$

$$i_{Ls}(t_2) = \frac{1}{2}\left(\frac{V_{HV}}{L_s}(1 + d_B - 2 \cdot \phi - 2 \cdot \phi_{HV}) + \frac{N \cdot V_C}{L_s}(-1 + d_B)\right)T_s \tag{13}$$

$$i_{Ls}(t_3) = \frac{1}{2}\left(\frac{V_{HV}}{L_s}(2 - d_B - 2 \cdot \phi - 2 \cdot \phi_{HV}) + \frac{N \cdot V_C}{L_s}(-1 + d_B)\right)T_s \tag{14}$$

where:

$$V_C = V_{C1} = V_{C2} = \frac{V_{12}}{1 - d_B} \tag{15}$$

The power of HV-port, P_{HV}, is calculated from the product of v_{ab} and i_{Ls}. From (10) and (11), P_{HV} is generalized as

$$\begin{aligned} P_{HV} &= \int_{T_s} v_{ab} \cdot i_{Ls}(t)dt \\ &= \frac{N \cdot V_{HV} \cdot V_C}{T_s L_s}\begin{pmatrix} d_B^2 - d_B + 5\phi_{HV}^2 - 7\phi_{HV} \\ +4\phi^2 - 6\phi + 8\phi \cdot \phi_{HV} + 2.5 \end{pmatrix} \end{aligned} \tag{16}$$

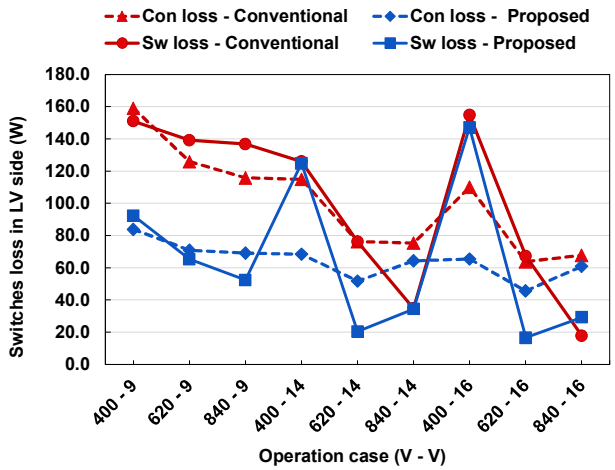

Fig. 8 Comparision of LV side switch-loss between the conventional and proposed three-port APM.

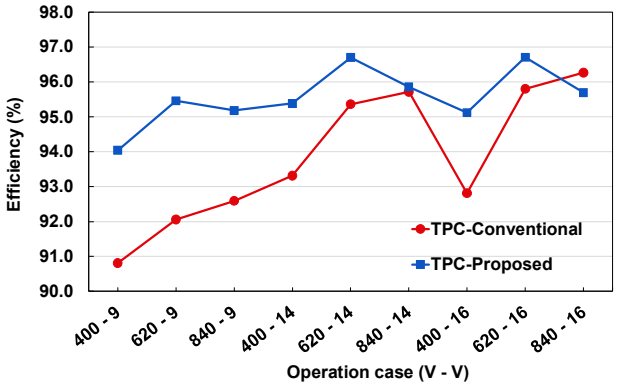

Fig. 9 Comparition of calculated efficiency between the conventional and proposed three-port APM.

III. Performance Comparison of Proposed- with Conventional- Three-Port Converter for Dual Auxiliary Voltage EV Application

TABLE II shows the designed specifications of the dual auxiliary voltage system in the EV application. In this system, the HV port and V_{12} port are batteries that require wide voltage ranges, while the V_{48} port is a fixed voltage to power the load. For a 6.1kW power converter, the current rating of the LV side switches is too large, and single switches can not handle it. Therefore, the multi-leg LV side concept is used, as shown in Fig. 7. The phase between each leg at the top or bottom is set to 180°, effectively reducing the current stress on output capacitors (C_{o1}, C_{o2}) by two times due to interleaving.

To show the performance of the proposed converter, comparisons are conducted. The design specifications are shown in TABLE II, and the comparison of component ranting and designed parameters is shown in TABLE III. It can be seen that the proposed converter requires smaller filter inductances (L_1, L_2, L_3, L_4), resulting in smaller inductor volume. Additionally, the LV switches have smaller voltage stress, resulting in reduced conduction and switching losses. Although the used switches are different, the switching loss is mostly depend on the voltage stress and turn off current. Fig. 8

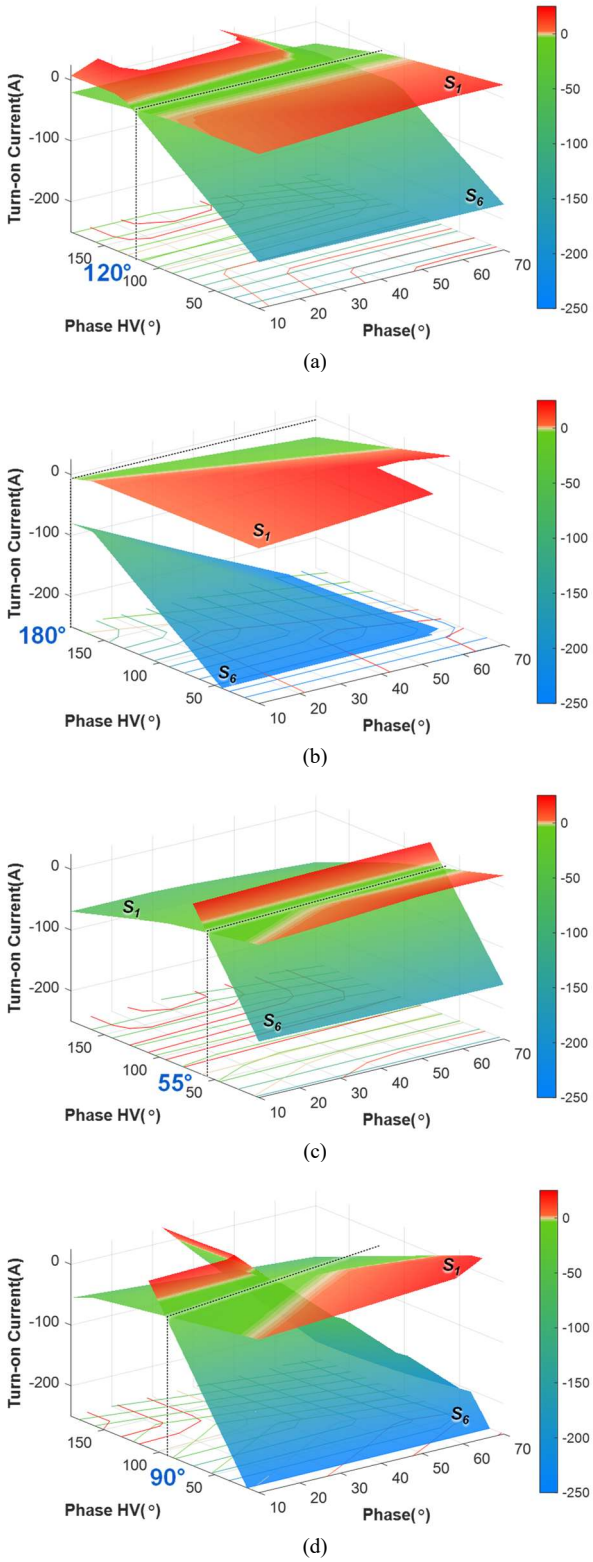

Fig. 10 Soft switching characteristic of the proposed converter: (a) V_{HV} = 400V and V_{12} = 9V, (b) V_{HV} = 400V and V_{12} = 16V, (c) V_{HV} = 840V and V_{12} = 9V, (d) V_{HV} = 840V and V_{12} = 16V.

shows the LV side switch loss, where the switching loss is significantly reduced due to the lower voltage stress. The conduction loss is also reduced due to the use of lower $R_{DS,on}$

switches. As a result, the efficiency of the proposed converter is significantly increased, as shown in Fig. 9. At 9V, the conventional topology uses a duty cycle of 0.81. In contrast, the proposed converter uses the duty cycle of 0.68, which significantly reduces the turn-off current and circulating current. Therefore, the efficiency of the proposed converter is significantly improved at 9V.

IV. Soft Switching Analysis of Proposed Converter

The proposed three-port converter has three control variables: ϕ, ϕ_{HV}, and d_B. The power voltage regulation between the 48V and 12V ports is determined by the duty cycle d_B, and the power flow between the HV side and the LV side is controlled by phase-shift ϕ. Therefore, there is only an HV phase-shift, ϕ_{HV}, that can be used to optimize the soft switching range. To simplify the analysis of the soft-switching condition, the effect of deadtime and switches junction capacitors is ignored. And when the switch turn-on current is smaller than zero, the ZVS is realized. From Fig. 5(b), it can be seen that switch S_1 makes it difficult to achieve ZVS on the HV side, while switch S6 makes it difficult to achieve ZVS on the LV side. Therefore, the ZVS condition of switch S_1 and switch S_6 is analyzed.

Since the HV port voltage range is 400V-840V and the 12V port voltage is 9V-16V, Fig. 10 shows the soft switching characteristic of the proposed three-port converter under four operating boundary voltage conditions for HV ,12V ports, and a fixed voltage for the 48V port, and the entire power range. The switches cannot achieve ZVS turn-on at the red region. In Fig. 10, as the phase shift (ϕ) is increases, the power is increases. By optimizing the HV phase-shift (ϕ_{HV}) the switches can achieve ZVS turn-on under the entire voltage and power range. In Fig. 10(a), with selected HV phase-shift (ϕ_{HV}) is set to 120°, the proposed converter can achieve ZVS for the entire power range at V_{HV} = 400V and V_{12} = 9V. Similarly, HV phase-shift is optimized for other voltage conditions in Fig. 10(b,c,d).

IV. Experimental Results

To validate the proposed converter, a 6.1kW, 100kHz prototype has been built, as shown in Fig. 11. The detailed specification of the proposed three-port converter is shown in TABLE I, while the design component parameters of the prototype are provided in TABLE III. The proposed converter used the top-colling surface-mount device (SMD) SiC switches provided by Infineon, as shown in Fig. 11(b,c). Top-colling switches not only reduce the manufacturing process but also have a 35% reduction of thermal resistance compared to bottom-colling switches [31]. Additionally, the prototype designs the height of all components is 24mm, achieving a power density of 9.14kW/L. Fig. 12 shows the 12V battery charging profile of the proposed APM. Since the auxiliary power is divided into 12V and 48V, the maximum current of the 12V port is only 150A.

Fig. 13, 14, and 15 show the experimental waveforms of the proposed converter under different voltage conditions. The experimental power conditions of the 12V port are obtained

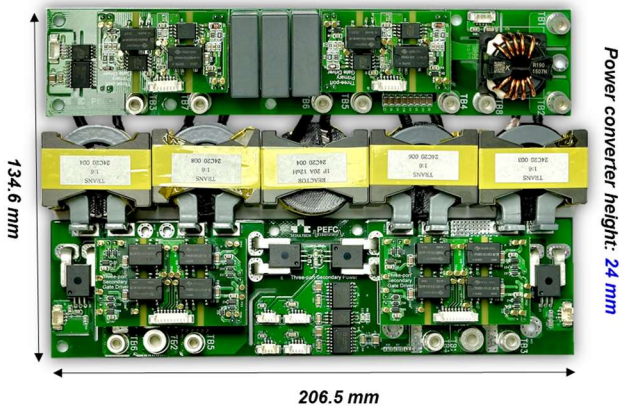

(a)

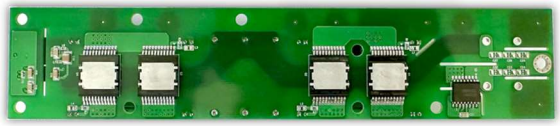

(b)

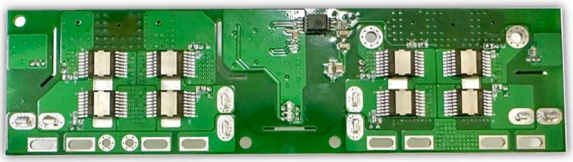

(c)

Fig. 11 Prototype of the proposed APM converter: (a) Top view prototype, (b) bottom view of HV side PCB, and (c) bottom view of LV side PCB.

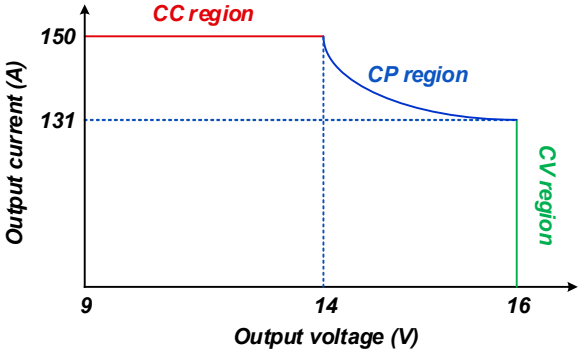

Fig. 12 12V battery charging profile for the proposed APM converter.

from the battery charging profile of the proposed APM, as shown in Fig. 12, while the power condition of the 48V port is fixed at 4kW. The ZVS condition of HV side switches can be observed through the series inductor current waveforms (i_{Ls}), it can be seen that all HV side switches could achieve full ZVS under different voltages. For the low-side switches, the ZVS condition can be realized through the drain-source voltage and gating signal. Due to symmetrical topology, the ZVS condition is identical for all legs, so only one-leg voltage waveforms are provided. Fig. 13, 14, and 15 show that the gating voltage begins to rise after the drain-source voltage decreases to zero, indicating that the low-side switches can achieve full ZVS across a wide voltage range, verifying the converter can achieve the entire ZVS range. Fig 16 shows the

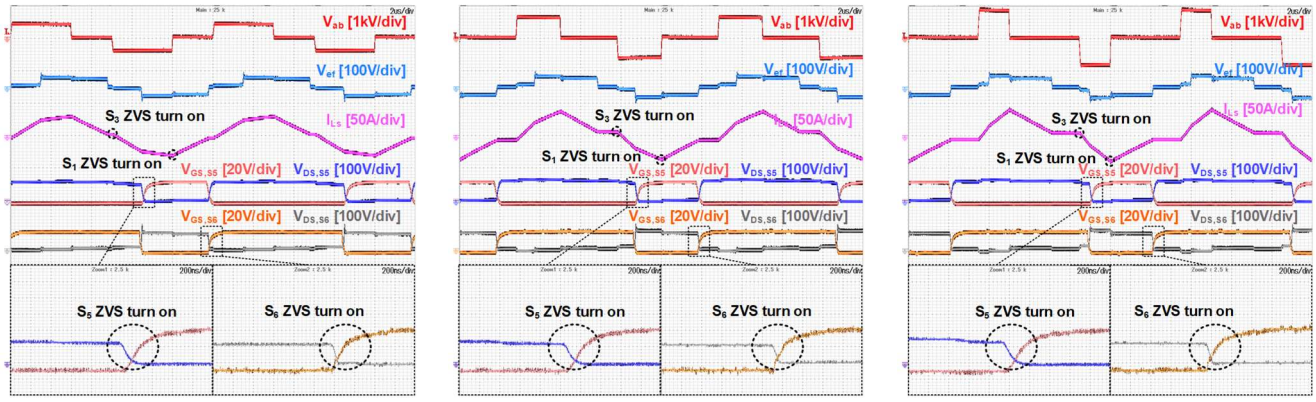

(a) (b) (c)

Fig. 13. Experiment waveforms of proposed APM at V_{12} = 9V (a) V_{HV} = 400V, (b) V_{HV} = 620V, (c) V_{HV} = 840V.

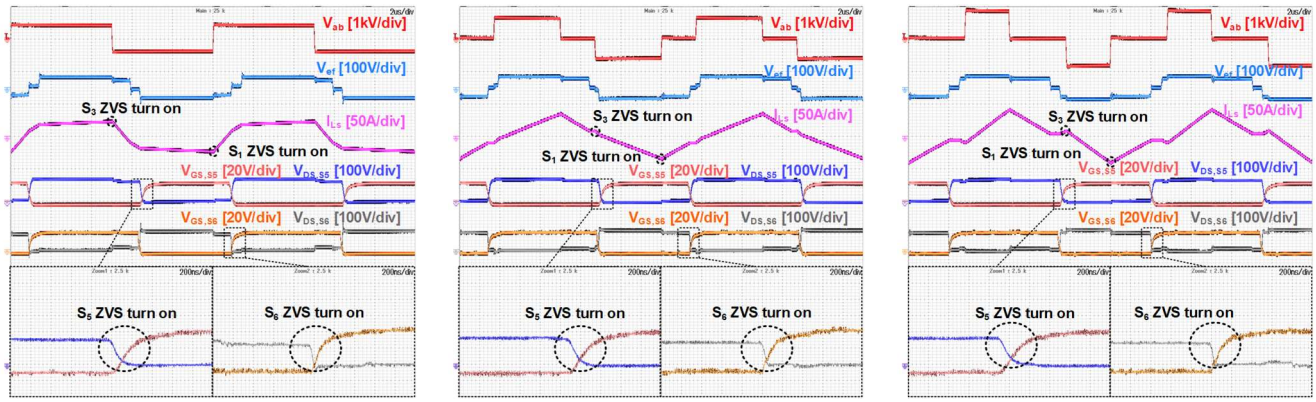

(a) (b) (c)

Fig. 14. Experiment waveforms of proposed APM at V_{12} = 14V (a) V_{HV} = 400V, (b) V_{HV} = 620V, (c) V_{HV} = 840V.

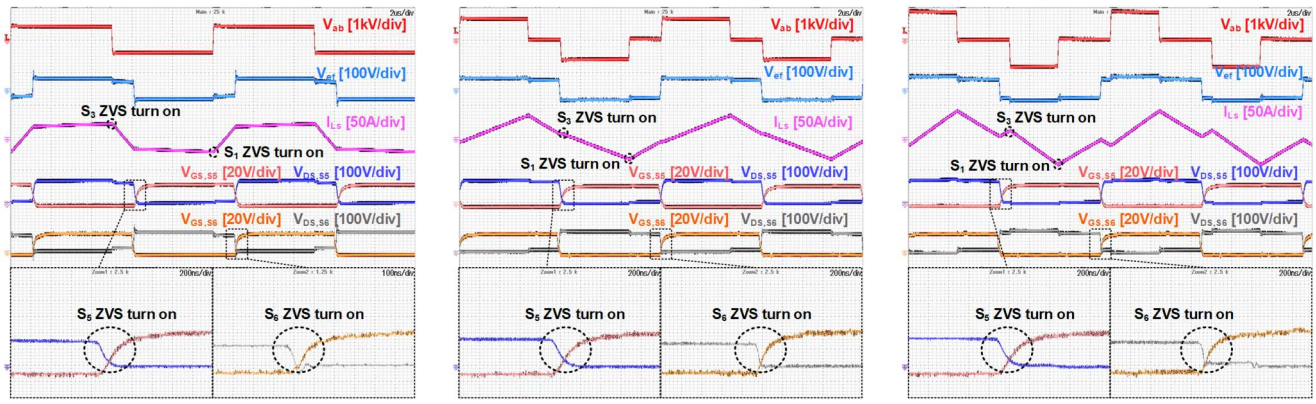

(a) (b) (c)

Fig. 15. Experiment waveforms of proposed APM at V_{12} = 16V (a) V_{HV} = 400V, (b) V_{HV} = 620V, (c) V_{HV} = 840V.

measured efficiencies of the proposed three-port APM under various conditions according to the battery charging profile. With a maximum current of 150A at 9V, the maximum operating power is 5.35kW (1.35kW to 12V port and 4kW to 48V port). When 12V port is at 14V and 16V, the maximum power is 6.1kW. The peak efficiency of the prototype is 96.6% at 400V-48V-14V voltage and 2.4kW power conditions. Efficiencies were measured using a Yokogawa WT 3000. The loss breakdown of the proposed APM under nominal conditions is shown in Fig. 17. Fig. 18 and Fig. 19 show the thermal measurement of the proposed APM prototype at worst case (V_{HV} = 400V, V_{48} = 48V, V_{12} = 14V, P_{HV} = 5.1kW ~ 83.6%,, P_{48} = 3.5kW, P_{12} = 1.6kW). Fig. 18 shows the thermal graph of the magnetic components, the winding of the transformer is the hottest at 60.7°C. Fig. 18 shows the switches thermal performance. The secondary switch S_5 is the hosttest switch of 75.8°C.

Table IV provides a comparison of the proposed three-port APM with previous works in [12],[13],[15], [17], and [23]. The APM in [12] employs two separate converters and is designed for the 400V battery class, achieving a power density of 2.6kW/L. To improve the efficiency of the power transfer from the HV battery to the LV battery, the APMs in [17], and [23] used a TAB converter. In [23], the peak efficiency

This article has been accepted for publication in IEEE Transactions on Power Electronics. This is the author's version which has not been fully edited and content may change prior to final publication. Citation information: DOI 10.1109/TPEL.2024.3508085

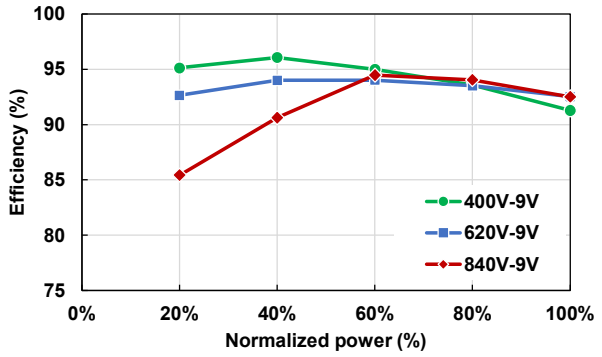

(a)

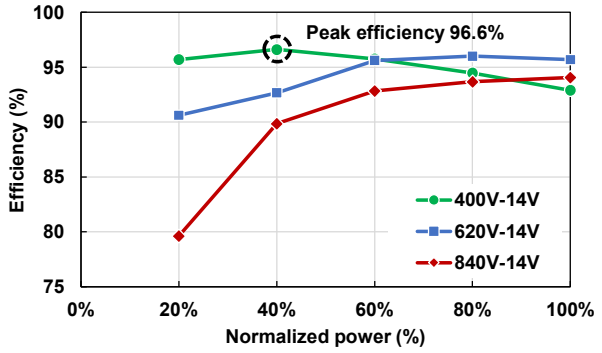

(b)

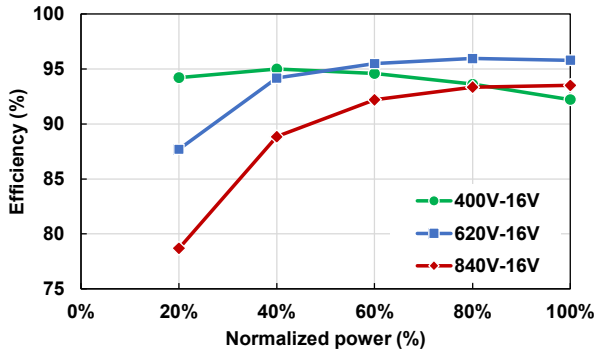

(c)

Fig. 16. Measured efficiencies of the proposed APM (measured by Yokogawa WT3000) (a) V_{12} = 9V, (b) V_{12} = 14V, (c) V_{12} = 16V.

achieves 96.3%. However, the power density of these prototypes is not provided. Since the power coupling can be solved by a current-fed DAB converter, the three-port APM in [13], and [15] use a current-fed DAB-based design, achieving a power density of 3.8kW/L. However, due to the operating duty being far from 0.5, the peak efficiency is only 95%, resulting from high conduction loss and switching loss. The proposed three-port APM shifts the operating duty range closer to 0.5, achieving a peak efficiency of 96.6% and a power density of 9.14kW/L.

V. Conclusion

A dual floating DAB three-port converter has been proposed, which combines a dual floating buck-boost converter with a DAB converter. The high voltage gain of the DFB conver ter keeps the duty range around 0.5, reducing the

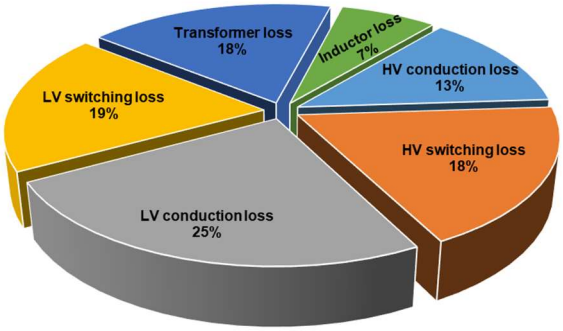

Fig. 17. Loss breadown of the proposed APM (V_{HV} = 620V, V_{48} = 48V, V_{12} = 14V, P_{HV} = 6.1kW, P_{48} = 4kW, P_{12} = 2.1kW).

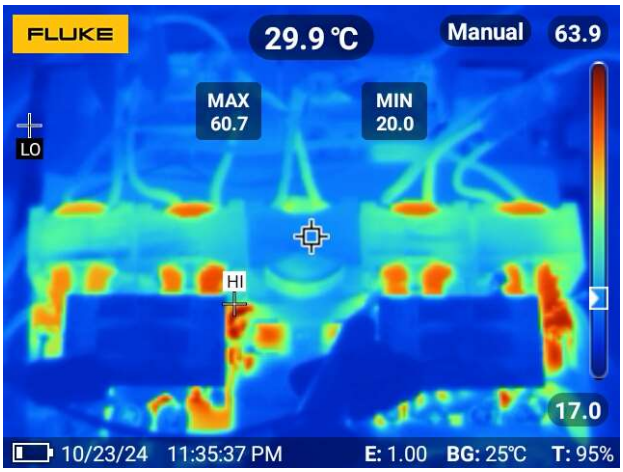

Fig. 18. Measured Thermal Graph of the magnetic componets (V_{HV} = 400V, V_{48} = 48V, V_{12} = 14V, P_{HV} = 5.1kW ~ 83.6%,, P_{48} = 3.5kW, P_{12} = 1.6kW).

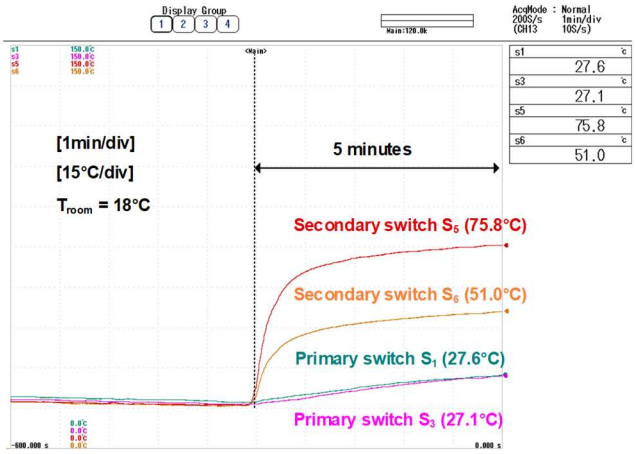

Fig. 19. Switch thermal test of the proposed APM (V_{HV} = 400V, V_{48} = 48V, V_{12} = 14V, P_{HV} = 5.1kW ~ 83.6%, P_{48} = 3.5kW, P_{12} = 1.6kW).

filter size, and circulating current, and increasing power transfer capability to the high voltage side. The comparisons of output current ripple, turns-off current, circulating current, and efficiency have been performed to show the effectiveness of the proposed converter. A 6.1kW, 100kHz prototype of the proposed TPC has been built to validate the performance of

TABLE IV
Comparision of three-port APM for dual auxiliary voltage system

	[12]	[17]	[23]	[13]	[15]	**Proposed**
Topology	Separated two converters	Triple active bridge	Resonant based triple active bridge	Half bridge current fed DAB	Current fed DAB	Dual floating based DAB
Power Rating	13kW	1.5 kW	6 kW	1.4 kW	0.75 kW	6.1 kW
HV-port Voltage	225 ~ 430V	300 V	400 ~ 800 V	250 ~ 400 V	180 ~ 210 V	400 ~ 840 V
48V-port Voltage	32 ~ 52V	42 V	46 ~ 50 V	42 V	48 V	48 V
12V-port Voltage	9 ~ 16V	14 V	10 ~ 14 V	14 V	12 V	9 ~ 16 V
Peak Efficiency	-	91.7%	96.3%	-	95%	96.6%
Switching Frequency	-	100 kHz	100kHz	22 kHz	175 kHz	100 kHz
Power Density	2.6 kW/L*	-	-	-	3.8 kW/L**	9.1 kW/L**

Noted: * the power density including housing
** the power density excluding housing

the proposed converter. Experimental results show the operating waveform under a wide high voltage port range of 400V-840V and a 12V port voltage range of 9V-16V, verifying that all switches can achieve ZVS turns on. The prototype achieves a power density of 9.1kW/L and a peak efficiency of 96.6%.

ACKNOWLEDGMENT

This study was supported by the Research Program funded by the SeoulTech (Seoul National University of Science and Technology).

The authors thank Infineon for support of the sample switch devices.

REFERENCES

[1] U.S. Department of Energy, “U.S. DRIVE electrical and electronics technical team roadmap,” Washington, DC, USA, Oct. 2017. [Online], Available: https://www.energy.gov/sites/prod/files/2017/11/f39/EETT%20Roadmap%2010-27-17.pdf.

[2] I. Aghabali, J. Bauman, P. J. Kollmeyer, Y. Wang, B. Bilgin and A. Emadi, "800-V Electric Vehicle Powertrains: Review and Analysis of Benefits, Challenges, and Future Trends," in IEEE Transactions on Transportation Electrification, vol. 7, no. 3, pp. 927-948, Sept. 2021, doi: 10.1109/TTE.2020.3044938.

[3] Kotb, R.; Chakraborty, S.; Tran, D.-D.; Abramushkina, E.; El Baghdadi, M.; Hegazy, O. Power Electronics Converters for Electric Vehicle Auxiliaries: State of the Art and Future Trends. Energies 2023, 16, 1753. https://doi.org/10.3390/en16041753.

[4] C. Wang, P. Zheng and J. Bauman, "A Review of Electric Vehicle Auxiliary Power Modules: Challenges, Topologies, and Future Trends," in IEEE Transactions on Power Electronics, vol. 38, no. 9, pp. 11233-11244, Sept. 2023, doi: 10.1109/TPEL.2023.3288393.

[5] D. Lee, H. -P. Kieu, J. Kim, S. Choi, S. Kim and W. Martinez, "A GaN-Based Improved Zeta Converter With Integrated Planar Transformer for 800-V Electric Vehicles," in IEEE Transactions on Industrial Electronics, doi: 10.1109/TIE.2024.3390728.

[6] V. -C. Bui, M. -K. Nguyen, T. -D. Duong, D. -V. Vo, Y. -C. Lim and J. -H. Choi, "A Novel Isolated DC–DC Converter for High Step-Down Applications," in IEEE Access, vol. 11, pp. 81545-81562, 2023, doi: 10.1109/ACCESS.2023.3298022.

[7] H. -P. Kieu, D. B. -H. Nguyen and S. Choi, "An All-in-one Magnetic Structure for Entire ZVS Range Auxiliary Power Module in Electrical Vehicles," in IEEE Transactions on Power Electronics, doi: 10.1109/TPEL.2024.3412135.

[8] S. -W. Jeong, S. -H. Lee, D. -H. Kwon, J. -Y. Kim and J. -K. Kim, "Two-Transformer Phase-Shift Full-Bridge Converter With a New Rectifier for Reducing Conduction Loss," in IEEE Transactions on Power Electronics, vol. 38, no. 12, pp. 15634-15644, Dec. 2023, doi: 10.1109/TPEL.2023.3303917.

[9] H. -P. Kieu, D. B. -H. Nguyen, D. Lee and S. Choi, "All-in-one Magnetic Structure for PSFB converter with Current Doubler Rectifier," 2024 IEEE Applied Power Electronics Conference and Exposition (APEC), Long Beach, CA, USA, 2024, pp. 875-880, doi: 10.1109/APEC48139.2024.10509124.

[10] L. Zhu, H. K. Bai, A. Brown and M. McAmmond, "Dynamic Process Analysis of a High-Power Bidirectional DC/DC Converter for Electric Vehicles," 2020 IEEE Energy Conversion Congress and Exposition (ECCE), Detroit, MI, USA, 2020, pp. 864-870, doi: 10.1109/ECCE44975.2020.9235909.

[11] L. Zhu, H. Bai, A. Brown and M. McAmmond, "Design a 400 V–12 V 6 kW Bidirectional Auxiliary Power Module for Electric or Autonomous Vehicles With Fast Precharge Dynamics and Zero DC-Bias Current," in IEEE Transactions on Power Electronics, vol. 36, no. 5, pp. 5323-5335, May 2021, doi: 10.1109/TPEL.2020.3028361.

[12] Fraunhofer. “ Bidirectional HV – 48V – 12V DC/DC Converter” 3-Port-Bordnetz-DC/DC-Wandler. [Online]. Available: https://www.iisb.fraunhofer.de/en/research_areas/vehicle_electronics/on-board-converters.html, Accessed: Jul. 10, 2024.

[13] G. -J. Su and L. Tang, "A Reduced-Part, Triple-Voltage DC–DC Converter for EV/HEV Power Management," in IEEE Transactions on Power Electronics, vol. 24, no. 10, pp. 2406-2410, Oct. 2009, doi: 10.1109/TPEL.2009.2026989.

[14] M. Ishigaki, K. Ito, S. Tomura and T. Umeno, "A new isolated multi-port converter using interleaving and magnetic coupling inductor technologies," 2013 Twenty-Eighth Annual IEEE Applied Power Electronics Conference and Exposition (APEC), Long Beach, CA, USA, 2013, pp. 1068-1074, doi: 10.1109/APEC.2013.6520432.

[15] S. Inoue, K. Itoh, M. Ishigaki and T. Sugiyama, "Magnetically integrated isolated bidirectional three-port DC-DC converter," 2017 19th European Conference on Power Electronics and Applications (EPE'17 ECCE Europe), Warsaw, Poland, 2017, pp. P.1-P.10, doi: 10.23919/EPE17ECCEEurope.2017.8099051.

[16] Y. Li, Y. Wang, Y. Guan and D. Xu, "Design and Optimization of High-Gain Bidirectional DC–DC Converter for Electric Vehicles," in IEEE Transactions on Power Electronics, vol. 38, no. 9, pp. 11221-11232, Sept. 2023, doi: 10.1109/TPEL.2023.3285627.

[17] C. Zhao, S. D. Round and J. W. Kolar, "An Isolated Three-Port Bidirectional DC-DC Converter With Decoupled Power Flow Management," in IEEE Transactions on Power Electronics, vol. 23, no. 5, pp. 2443-2453, Sept. 2008, doi: 10.1109/TPEL.2008.2002056.

[18] H. -P. Kieu, N. -Q. Do and S. Choi, "A New Bidirectional Three Port DC-DC Converter for Dual Auxiliary Voltage in EV Application," 2024 IEEE 10th International Power Electronics and Motion Control Conference (IPEMC2024-ECCE Asia), Chengdu, China, 2024, pp. 1870-1874, doi: 10.1109/IPEMC-ECCEAsia60879.2024.10567112.

[19] S. Choi and H. P. Kieu, “Three-port converter,” Korean Patent pending 10-2024-0064150, 2024.

[20] M. Uno, M. Sato, Y. Tada, S. Iyasu, N. Kobayashi and Y. Hayashi, "Partially Isolated Multiport Converter With Automatic Current Balancing Interleaved PWM Converter and Improved Transformer Utilization for EV Batteries," in IEEE Transactions on Transportation Electrification, vol. 9, no. 1, pp. 1273-1288, March 2023, doi: 10.1109/TTE.2022.3175032.

[21] N. -Q. Do, C. Lee, J. Kim, H. -P. Kieu and S. Choi, "800V/48V/12V 6kW resonant dc-dc converter with dual transformers for Electric Vehicles," 2024 IEEE 10th International Power Electronics and Motion Control Conference (IPEMC2024-ECCE Asia), Chengdu, China, 2024, pp. 1959-1963, doi: 10.1109/IPEMC-ECCEAsia60879.2024.10567416.

[22] N. Keshmiri, G. A. Mudiyanselage, S. Chakkalakkal, K. Kozielski, G. Pietrini and A. Emadi, "Design and Control Methodology of a Three-Port Resonant Converter for Electric Vehicles," in IEEE Open Journal of the Industrial Electronics Society, vol. 3, pp. 650-662, 2022, doi: 10.1109/OJIES.2022.3215772.

[23] G. Abeysinghe Mudiyanselage et al., "Phase-Shift and Duty-Ratio Control Optimization of a 6 kW Three-Port Resonant DC-DC Converter for Dual Auxiliary Voltage EV Applications," in IEEE Transactions on Power Electronics, doi: 10.1109/TPEL.2024.3422408.

[24] M. Su, Q. Ouyang, G. Deng, G. Xu, Y. Sun and W. Xiong, "Modified Topology and PWM Modulation for Bidirectional LLC-DCX Converter With Center-Tapped Transformer," in IEEE Transactions on Transportation Electrification, vol. 8, no. 3, pp. 3907-3920, Sept. 2022, doi: 10.1109/TTE.2022.3152838.

[25] D. Choi, J. -S. Kim, S. -H. Choi, Y. Jeong and G. -W. Moon, "A New Voltage Distribution Strategy in Input-Series Connected Dual Active Bridge Converters," 2024 IEEE 10th International Power Electronics and Motion Control Conference (IPEMC2024-ECCE Asia), Chengdu, China, 2024, pp. 1336-1339, doi: 10.1109/IPEMC-ECCEAsia60879.2024.10567739.

[26] P. R. Prakash, A. Nabih, S. Wang, P. P. Hieu, Y. Ruan and Q. Li, "GaN-Based 400V/48V DC-DC Converter with 97% Efficiency and PCB Magnetics for Automotive Applications," 2023 IEEE Applied Power Electronics Conference and Exposition (APEC), Orlando, FL, USA, 2023, pp. 3201-3208, doi: 10.1109/APEC43580.2023.10131189.

[27] Zhou, K.; Liu, Y.; Wu, X. Research on Wide Input Voltage LLC Resonant Converter and Compound Control Strategy. Electronics 2022, 11, 3379. https://doi.org/10.3390/electronics11203379.

[28] Y. Wang, Y. Li, Y. Guan and D. Xu, "Topology and Control Optimization of Bidirectional DC/DC Converter for Electric Vehicles," in IEEE Journal of Emerging and Selected Topics in Power Electronics, vol. 12, no. 1, pp. 257-268, Feb. 2024, doi: 10.1109/JESTPE.2023.3278718.

[29] Infineon, "48V 12V DC-DC converter" *48 V Systems for EVs & Mild Hybrids*. [Online]. Available: https://www.infineon.com/cms/en/applications/automotive/powertrain-systems/mild-hybrid-48v-mhev/48v-12v-dc-dc-converter/ Accessed: Jul. 10, 2024.

[30] Vicor, "Electric Vehicles: 48V is the new 12V". [Online]. Available: https://www.vicorpower.com/resource-library/articles/automotive/electrified-vehicles-48v-is-the-new-12v Accessed: Jul. 10, 2024.

[31] Valeo, "48V to 12V DCDC Converter" *Catalogue*, 2023. [Online]. Available: https://www.valeo.com/en/catalogue/pts/48v-to-12v-dcdc-converter/ Accessed: Jul. 10, 2024.

[32] B. Li, W. Qin, Y. Yang, Q. Li, F. C. Lee and D. Liu, "A High Frequency High Efficiency GaN Based Bi-Directional 48V/12V Converter with PCB Coupled Inductor for Mild Hybrid Vehicle," 2018 IEEE 6th Workshop on Wide Bandgap Power Devices and Applications (WiPDA), Atlanta, GA, USA, 2018, pp. 204-211, doi: 10.1109/WiPDA.2018.8569067.

[33] D. -V. Bui, H. Cha and V. -C. Nguyen, "Asymmetrical PWM Series-Capacitor High-Conversion-Ratio DC–DC Converter," in IEEE Transactions on Power Electronics, vol. 36, no. 8, pp. 8628-8633, Aug. 2021, doi: 10.1109/TPEL.2021.3056659.

[34] H. N. Tran, T. -T. Le, H. Jeong, S. Kim, H. -P. Kieu and S. Choi, "High Power Density DC-DC Converter for 800V Fuel Cell Electric Vehicles," 2021 IEEE 12th Energy Conversion Congress & Exposition - Asia (ECCE-Asia), Singapore, Singapore, 2021, pp. 2224-2228, doi: 10.1109/ECCE-Asia49820.2021.9479257.

[35] Infineon. "Infineon QDPAK and DDPAK top-side cooling packages registered as JEDEC standard for high-power applications" Market News, 2023. [Online]. Available: https://www.infineon.com/cms/en/aboutinfineon/press/marketnews/2023/INFPSS202302-057.html, Accessed: Jul. 10, 2024.